CrossMark

RESEARCH PAPER

Electroosmotic flow profile distortion due to Laplace pressures at the end reservoirs

Arturo Bianchetti[1] · **Santiago Hernández Sánchez[2]** · **Juan Martín Cabaleiro[2,3]**

Abstract The build-up of pressure-driven backflows is a known drawback to electroosmotic plug flow. We have studied the characteristic time constant of these pressure gradients build-up as a function of various geometrical variables of the problem through μPIV measurements. Previous models based on hydrostatic pressure difference (syphoning) cannot explain the dynamics of our experimental results. We have developed a model that relates these pressure-driven backflows to Laplace pressures, due to changes in the interface radii of curvature at the reservoirs. This model leads to an equation which was solved both numerically and, after linearisation, analytically. The characteristic time constants obtained show much better agreement with experimental data. Therefore, this model allows for predicting the time during which an acceptable electroosmotic flow profile will last for a given microchannel–reservoir design.

Keywords Electroosmotic flow · Adverse pressure gradient · Laplace pressures · Electrokinetics

✉ Arturo Bianchetti
   abianchetti@gmail.com

1   Electronics and Information Systems, National Institute
    of Industrial Technology, P.O. Box B1650WAB,
    B1650KNA San Martín, Argentina

2   CONICET-Fluid dynamics Laboratory, Faculty
    of Engineering, University of Buenos Aires, Av. Paseo Colón
    850, Buenos Aires, Argentina

3   Micro and Nanofluidics and Plasma Laboratory, Faculty
    of Engineering, Marina Mercante University, Av. Rivadavia
    2258, Buenos Aires, Argentina

1 Introduction

Electrokinetically driven flows have been used to move liquids in microfluidic devices for more than two decades with many applications, due to the simplicity of construction and operation (Li 2004; Kirby 2010; Squires and Quake 2005; Ghosal 2004). Typically, the velocity profile that develops in electroosmotic flow (EOF) in the absence of pressure gradients is flat, known as plug velocity profile. This kind of velocity profile is particularly useful for pumping (without moving parts) and for electrophoretic separations in laboratory on a chip devices. In electrophoretic separation applications, EOF does not add any significant shear induced axial dispersion (Taylor-Aris dispersion) to the analyte. Band broadening in this case is purely due to axial molecular diffusion (Ghosal 2004). Concerning pumping applications, EOF velocities do not depend on the microchannel dimensions, in striking contrast with pressure-driven flows, whose velocity decreases with the second power of channel size (Squires and Quake 2005). That is, pressure-driven flows are inefficient and difficult to build at small scales for transporting ionic species. However, any source of distortion of the EOF profile may produce undesired effects, namely, to reduce the flowrate (unwanted effect in pumping applications) and to result in strong band broadening due to Taylor-Aris dispersion (unwanted effect in electrophoretic separation applications). In practice, pressure-driven backflows develop, distorting the EOF velocity profile. In order to avoid or limit the unwanted effects mentioned previously, it is important to characterise the dynamics of the adverse pressure gradient driving the backflow. The microfluidic chips should be designed in order to work on a near plug-like profile during the time needed for the separation or pumping. Yan et al. (2007) presented a model relating these pressure-driven backflows to the height change in the

reservoirs, due to the net pumping from one reservoir to the other. This model could qualitatively explain the behaviour observed in the experiments, given that the flow from one reservoir to the other would produce an increase in the height of the reservoir receiving the fluid and a decrease in the other one. This height difference would in turn give rise to a pressure difference producing a counterflow, which increases as the height difference increases. At some point, this counterflow would completely compensate the electroosmotic flow. In this final equilibrium condition, the net flowrate is zero. The whole process may be characterised by a time constant. As we will show later in the results section, this model fails to describe our experimental results because the time constant value it produces is much larger than the one observed experimentally. Based on MacInnes et al. (2003), Yan et al. (2007) argue that, since they use identical reservoirs, the pressure jump across the liquid–gas interface is equal at both reservoirs and should balance each other. However, MacInnes et al. (2003) state that in order to avoid surface tension effects in the reservoirs they used large 50 mm diameter reservoirs to reduce the magnitude of the possible pressure errors. Moreover, Kirby and Hasselbrink (2004) also mentioned that pressure induced by modest interface curvatures (e.g. 2 mm diameter) can lead to appreciable errors. Sinton et al. (2003a, b) state that Laplace pressure originating from differential meniscus curvatures in the reservoirs was found to be the most significant source of such pressure disturbances in a microfluidic-cross chip, in agreement with the results of Crabtree et al. (2001).

In line with these authors, we present in this work a different time-dependent model which relates the instantaneous pressure-driven backflow, to the Laplace pressure jump across the liquid–gas interface, in each reservoir, at the extremities of a rectangular cross-section microchannel. We compare the results of this model with μPIV velocity measurements finding a much better agreement than with the use of the model by Yan et al. (2007). Moreover, the time constants found both experimentally and theoretically are much shorter than those found by Yan et al. (2007), showing that the undesired pressure-driven backflow arises much faster.

2 Laplace pressures' based model

The model is derived from the Navier–Stokes (NS) equations, describing the flow in the microchannel (Fig. 1). Using a characteristic length l_c, a characteristic velocity U_c, a characteristic time t_c and the fluid's dynamic viscosity μ, the dimensionless NS equation becomes:

$$Re \frac{\partial \mathbf{u}^*}{\partial t^*} + Re\, \mathbf{u}^* \cdot \nabla^* \mathbf{u}^* = -\nabla^* p^* + \nabla^{*2} \mathbf{u}^* + \mathbf{f}_\mathbf{v}^*. \quad (1)$$
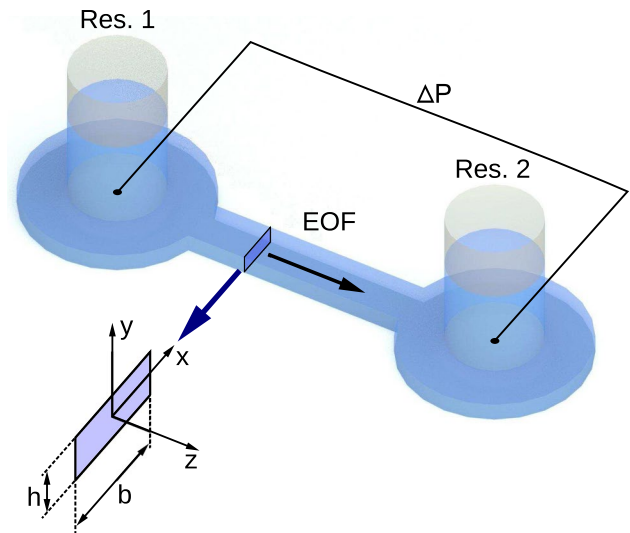

Fig. 1 Sketch of the microchannel and reservoirs, showing the Cartesian coordinates system used. ΔP is the pressure difference between the two reservoirs. h and b are the height and width of the microchannel

In this equation, $\mathbf{x}$, $\mathbf{u}$, p, t and $\mathbf{f}_\mathbf{v}$ are the position vector, velocity vector, pressure, time and volume force vector, respectively, so that we get the following nondimensional quantities:

$$\mathbf{x}^* = \frac{\mathbf{x}}{l_c}; \quad \mathbf{u}^* = \frac{\mathbf{u}}{U_c}; \quad \nabla^* = l_c \nabla; \quad \nabla^{*2} = l_c^2 \nabla^2;$$

$$t^* = \frac{t U_c}{l_c}; \quad p^* = \frac{p}{\mu U_c / l_c}; \quad \mathbf{f}_\mathbf{v}^* = \frac{\mathbf{f}_\mathbf{v}}{\mu U_c / l_c^2}; \quad (2)$$

$$Re = \frac{\rho U_c l_c}{\mu}.$$

where ρ is the fluid's density and μ is the fluid's dynamic viscosity. The last nondimensional quantity is the Reynolds number Re). In our problem, the timescale related to the boundary condition (the externally applied electric field) is longer than the convective timescale l_c / U_c; therefore, we chose the latter for the nondimensionalisation of time. Moreover, we consider here the unidirectional flow in a long constant cross-section channel so that the second term of Eq. 1 vanishes (Spurk and Aksel 2007). Nevertheless, the first term and second term are usually dropped to describe microflows (even in the case of nonunidirectional flows) because $Re \ll 1$. For example, if we take water, a characteristic length of $l_c = 100\,\mu\text{m}$ and a characteristic velocity $U_c = 1\,\text{mm/s}$, we get $Re = 10^{-1}$.

This leads to the Stokes equation, which is a linear partial differential equation. Considering that the volume force acting upon the fluid is a Coulomb force ($\mathbf{f}_\mathbf{v} = \rho_E \mathbf{E}$), the resulting equation is:

$$0 = -\nabla^* p^* + \nabla^{*2} \mathbf{u}^* + \frac{\rho_E \mathbf{E}}{\mu U_c / l_c^2}. \quad (3)$$

Its solution may be presented as the superposition of two others similarly to Dutta and Beskok (2001), or Santiago (2001):

$$\mathbf{u}^* = \mathbf{u}_{EOF}^* + \mathbf{u}_{\nabla p}^*. \tag{4}$$

The electroosmotic part of that solution, $\mathbf{u}_{EOF}^*$, requires solving the Poisson–Boltzmann equation for the electric potential due to the presence of the electrical double layer (EDL). Based on Burgreen and Nakache's (1964) work, Dutta and Beskok (2001) present a solution for the electroosmotic flow in a plane slit. Santiago (2001) also presents a solution in a plane slit, including the transient establishment of the velocity profile, and using Södermann and Jönsson's (1996) transient solution. Marcos et al. (2004) present an analytical solution in the case of a rectangular (2D) microchannel, by assuming low zeta potential (the Debye–Hückel approximation, i.e. using the linearised Poisson–Boltzmann equation). In general, the solution to the 2D nonlinear Poisson–Boltzmann equation requires a numerical approach (Li 2004). Nevertheless, in the absence of a pressure gradient, this solution leads to a plug-like velocity profile in which the velocity goes from zero at the walls to the characteristic Helmholtz–Smoluchowski electroosmotic velocity (u_{HS}). In the case of thin EDL (here we consider deionised—DI—water with a conductivity $\sigma \sim 5\,\mu\text{S/cm}$, which has a Debye length $\delta_D \sim 51\,\text{nm}$) compared to the channel height and width, the electric potential drops in a very thin region close to the walls, and it is possible to consider a slip model with the Helmholtz–Smoluchowski slip velocity (u_{HS}). Therefore, the plug-like velocity profile is simplified as a constant velocity profile, and the velocity profile inside the EDL is neglected:

$$\mathbf{u}_{EOF} = -\frac{\zeta\,\epsilon\,E_z}{\mu}\,\hat{k} = u_{HS}\,\hat{k}, \tag{5}$$

Here ζ is the zeta potential (the electric potential difference between the bulk and the Stern or compact layer Hunter 2001; Lyklema et al. 1995), ϵ is the fluid's permittivity and E_z is the magnitude of the externally applied electric field parallel to the wall. $\hat{k}$ is the unitary vector along the z axis (see Fig. 1).

The pressure gradient related part of the solution is, for a rectangular channel and in the quasi-static case presented here (Spurk and Aksel 2007):

$$\mathbf{u}_{\nabla p}(x, y, t) = -\frac{\partial p(z, t)}{\partial z}\frac{1}{2\,\mu}$$
$$\times \left[\frac{h^2}{4} - y^2 + \frac{8}{h}\sum_{n=1}^{\infty}\frac{(-1)^n}{m^3}\frac{\cos h(m\,x)}{\cos h(m\,b/2)}\cos(m\,y)\right]\hat{k}, \tag{6}$$

where $m = (2\,n - 1)\pi/h$.

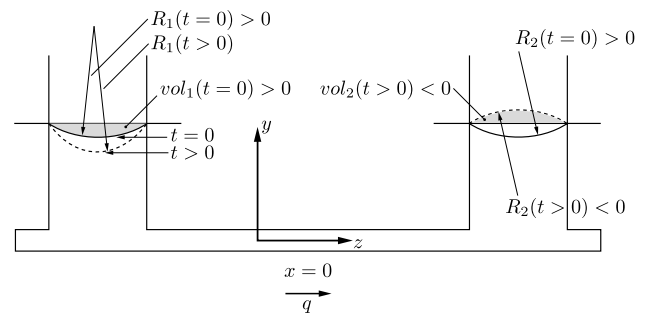The pressure gradient can be calculated as the pressure difference between the entrance and the exit of the

Fig. 2 Sketch of the interface at the reservoirs, at $t = 0$ s and at a later generic time $t > 0$ given a flowrate q. The volumes referred to as vol_1 and vol_2 are *shaded* in the figure

microchannel, divided by the channel's length L because in a unidirectional, constant cross-section flow, the pressure varies linearly with the axial coordinate;

$$\frac{\partial p(z, t)}{\partial z} = \frac{p_2(t) - p_1(t)}{L} = \frac{\Delta p(t)}{L}. \tag{7}$$

The pressure at the reservoirs is a function of the flowrate. As mentioned previously in this work, we present a model that relates the pressure at the base of the reservoirs to the Laplace pressure jump across the liquid–gas interface, in each reservoir. This hypothesis will be discussed further in Sect. 4.

The surface of the interface can be described at any point by two radii of curvature, R_i and R_j. In the case of small circular reservoirs, the interface will be approximately spherical in shape (Arthur and Adamson 1997). If we consider a spherical surface, these two radii are equal ($R_i = R_j = R_{curv}$). The Young–Laplace equation relates the pressure jump across the interface to these radii of curvature and the surface tension Γ:

$$p_0 - p_1 = \Gamma\left(\frac{1}{R_{i1}} + \frac{1}{R_{j1}}\right) = \frac{2\,\Gamma}{R_{curv_1}},$$
$$p_0 - p_2 = \Gamma\left(\frac{1}{R_{i2}} + \frac{1}{R_{j2}}\right) = \frac{2\,\Gamma}{R_{curv_2}}, \tag{8}$$
$$p_2 - p_1 = 2\,\Gamma\left(\frac{1}{R_{curv_1}} - \frac{1}{R_{curv_2}}\right).$$

where a positive curvature radius is associated with a positive volume and a negative curvature radius, to a negative volume. As indicated in Fig. 2, the volumes below a plane horizontal interface are considered positive and the ones above negative.

At any of the reservoirs, one can relate these volumes to the transported volume in a time interval dt:

$$\text{d}vol_1 = q\,\text{d}t,$$
$$\text{d}vol_2 = -q\,\text{d}t, \tag{9}$$

so that,

$$vol_1(t) = vol_1(0) + \int_0^t q(t)\,\mathrm{d}t,$$

$$vol_2(t) = vol_2(0) - \int_0^t q(t)\,\mathrm{d}t, \qquad (10)$$

where q is the flowrate and is defined positive when going from reservoir 1 to reservoir 2.

Moreover, these volumes can be related to the radius of curvature of the interface, considered here to be a spherical shell contained in a reservoir of radius R_{res} (Fig. 3).

The shaded volume shown in Fig. 3 can be calculated through the following integral:

$$vol_j(t) = 2\pi \int_0^{\phi_{\max_j}(t)} \left\{ \int_{\frac{R_{0_j}(t)}{\cos(\phi)}}^{R_{curv_j}((t)} r^2 \mathrm{d}r \right\} \sin(\phi)\,\mathrm{d}\phi, \quad (11)$$

where,

$$j = 1, 2;$$

$$\cos\left[\theta_{c_j}(t)\right] = \frac{R_{res}}{R_{curv_j}(t)} = \sin\left[\phi_{\max_j}(t)\right]; \qquad (12)$$

$$R_{0_j}(t) = R_{curv_j}(t) \cos\left[\phi_{\max_j}(t)\right].$$

After some rearranging, the result of Eq. 11 is,

$$R_{curv_j}^3 - \frac{\pi R_{res}^4}{4vol_j} R_{curv_j}^2 - \left(\frac{3vol_j}{4\pi} + \frac{\pi R_{res}^6}{12vol_j} \right) = 0, \qquad (13)$$

whose solution can be found in "Appendix".

Now, coming back to the flowrate,

$$q(t) = \int_{-\frac{h}{2}}^{\frac{h}{2}} \int_{-\frac{b}{2}}^{\frac{b}{2}} \mathbf{u}(x,y,t) \cdot \hat{k}\,\mathrm{d}x\mathrm{d}y = q_{EOF} + q_{\nabla p}(t), \quad (14)$$

where,

$$q_{EOF} = u_{EOF}bh;$$

$$q_{\nabla p}(t) = -K_1 \Delta p(t);$$

$$K_1 = \frac{D_h^2 bh}{32\mu L\, F\left(\frac{h}{b}\right)}; \quad D_h = \frac{2bh}{b+h};$$

$$F\left(\frac{h}{b}\right) = \left\{ 2\left(\frac{h}{b}+1\right)^2 \left[\frac{1}{3} - \frac{h}{b}\frac{64}{\pi^5}\sum_{n=1}^{\infty} \frac{\tan h\left(\frac{mb}{2}\right)}{(2n-1)^5} \right] \right\}^{-1}. \qquad (15)$$

Finally, according to this model the pressure drop is related to the radii of curvature at the reservoirs giving:

$$q(t) = q_{EOF} - K_2 \left(\frac{1}{R_{curv_1}(t)} - \frac{1}{R_{curv_2}(t)} \right), \qquad (16)$$
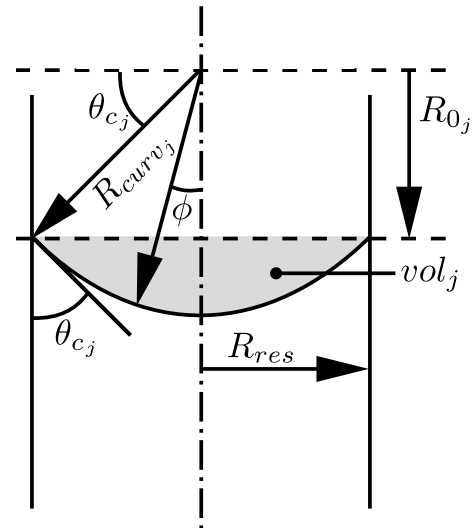
$$K_2 = 2K_1\Gamma.$$

Fig. 3 Sketch of the interface at one of the reservoirs of the microfluidic channel, showing the shaded volume vol_j (with $j = 1, 2$), the radius of curvature R_{curv_j}, the contact angle θ_{c_j}, the quantity R_{0_j} and the angle ϕ. These quantities are used in Eqs. 11 and 12
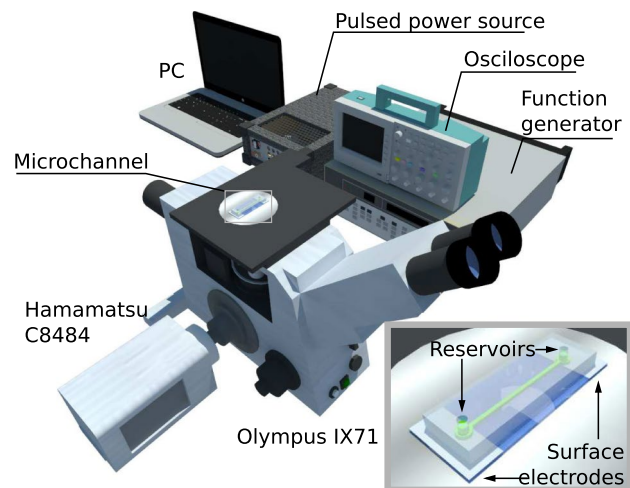

Fig. 4 Sketch of the experimental set-up consisting of an inverted epifluorescence microscope (IX71, Olympus, Japan), a LED light source (Multi TK-LED, Tolket S.R.L, Argentina), a PIV camera (C8484-05C, Hamamatsu Photonics, Japan), a digital oscilloscope, a function generator, a custom-made pulsed power source and a PC

Equation 16 can be numerically solved as shown in "Appendix".

Moreover, in order to compare our model to the one based on the height difference presented by Yan et al. (2007), Eq. 16 may be simplified to obtain the following analytical solution (see "Appendix"):

$$q(t) = q_{EOF} \exp\left(-\frac{t}{\tau} \right). \qquad (17)$$

$$\text{with} \quad \tau = \frac{2\pi R_{\mathrm{res}}{}^4 \mu L F\left(\frac{h}{b}\right)}{H(a_0)\Gamma D_h{}^2 bh}. \tag{18}$$

3 Experimental set-up

We have performed μPIV measurements at the mid-height a microchannel. The experimental set-up (Fig. 4) consists of an inverted epifluorescence microscope (IX71, Olympus, Japan), a LED light source (Multi TK-LED, Tolket S.R.L, Argentina), a PIV camera (C8484-05C, Hamamatsu Photonics, Japan), a digital oscilloscope, a function generator, a custom-made pulsed power source and a PC. This set-up allowed for the measurement of the velocity fields in the microchannel, as in classical μPIV Santiago et al. (1998), Wereley and Meinhart (2010), but with a LED light instead of a double pulsed laser light source.

Straight 40-mm-long microchannels were made by casting PDMS on a mould fabricated by classical photolithography (SU8 on silicon wafer) in a clean room. The microchannels' cross section was 55 μm tall by 79 μm wide. Engraved PDMS was then sealed with a PDMS coated microscope slide. We used native PDMS (no plasma cleaning treatment was performed, and the bonding was therefore reversible). Different diameter (0.3–2 mm), 5 mm tall reservoirs, were bonded to the microchannel at its extremities.

The power source allows for a square modulation of the electric potential (the maximum potential difference is 1 kV, up to 1 kHz). In this work, we used a square signal of known period (on–off, 50 % duty cycle) in the range of 2 s to 1200 s. The liquid was seeded with 500-nm polystyrene fluorescent microspheres (G500 Fluoro-Max Dyed Green Aqueous Fluorescent Particles, Thermo Fisher Scientific Inc., USA). The applied potential was 100V in all experiments. The wall zeta potential and the particles zeta potential were measured according to the procedure proposed in Yan et al. (2006). We obtained $\zeta_{\mathrm{wall}} = -105$ mV and $\zeta_{\mathrm{particle}} = -36$ mV. Both values are in agreement with the ones found in the literature for these materials (Kirby and Hasselbrink 2004; Sze et al. 2003; Xiong et al. 2012; Duffy et al. 2002). The velocity fields were registered focusing the microscope at the mid-height of the channel through a 40× objective (LUCPLFLN40XPH, Olympus, Japan), at a frequency between 2 and 5 velocity fields per second (that is, 2–5 double frame captures per second). The aperture of the 40× objective is 0.6 giving a depth of correlation of $2y_{\mathrm{corr}} = 6.3\ \mu$m (Bourdon et al. 2004).

During these experiments, the measured current through the microchannel was 50 nA. Considering an adiabatic process, the generated heat during the longest experiment correspond to a 0.3 °C increase, which represents a negligible zeta potential variation (Venditti et al. 2006).

The calculated total gas generation due to electrolysis (1 mol H_2 and 1/2 mol O_2) for the longest experiment represent approximately 5 and 6 % of the smallest reservoir and microchannel respectively. However, we did not observe bubbles in the microchannels during the experiments.

4 Results and discussion

Figure 5 shows typical velocity fields obtained with our experimental set-up. The top image (Fig. 5a) shows the velocity field during the initial times after the external electric field is applied, where pure electroosmotic plug flow can be observed. The middle image (Fig. 5b) corresponds to a time just before the end of the first semi-period. In this image, a combined electroosmotic and adverse pressure-driven flow is observed. The bottom image (Fig. 5c) corresponds to a time just after the beginning of the second semi-period (i.e. right after the external electric field has been turned off), where the flow is only pressure driven. The velocity profiles obtained along the channel (z direction) were space averaged to produce one velocity profile at each time. This z-averaged velocity profiles were then plotted against time as shown in Fig. 6. The phenomenon is periodic, as can be observed in this figure, allowing for phase averaging of the velocity profiles. This phase averaging produces better quality velocity profiles vs. time plots. Typical phase-averaged velocity profiles obtained are presented in Fig. 7 (phase averaging was done over 10 periods). As mentioned previously, during the first half period the external electric field is on, and during the second half period, it is off. This is the reason for the jump in the velocities at the half period. It is worth noting that during the first half period, the measured velocity is biased by the electrophoretic velocity of the particles. This work is focused on the dynamics of this problem and, therefore, on the time constant mainly which is not biased by the electrophoretic velocity.

Plotting the measured velocity at a given x coordinate and interpolating it with an exponential function allows for determining the system's time constant. The experimental data for $x = 0$, and $R_{\mathrm{res}} = 250\ \mu$m, and the interpolation are presented in Fig. 8. As expected, the time constant obtained is approximately the same for the first half period (electric field on) and for the second half period (electric field off).

The time constants determined with this method, for three different reservoirs used in this work, together with the time constants determined with the previously described "Laplace pressures" model, and the time constants determined with the model presented by Yan et al. (2007), are presented in Table 1. The remaining unknown parameters in the "Laplace pressures" model are the

(a) ⟶0.0005 m/s

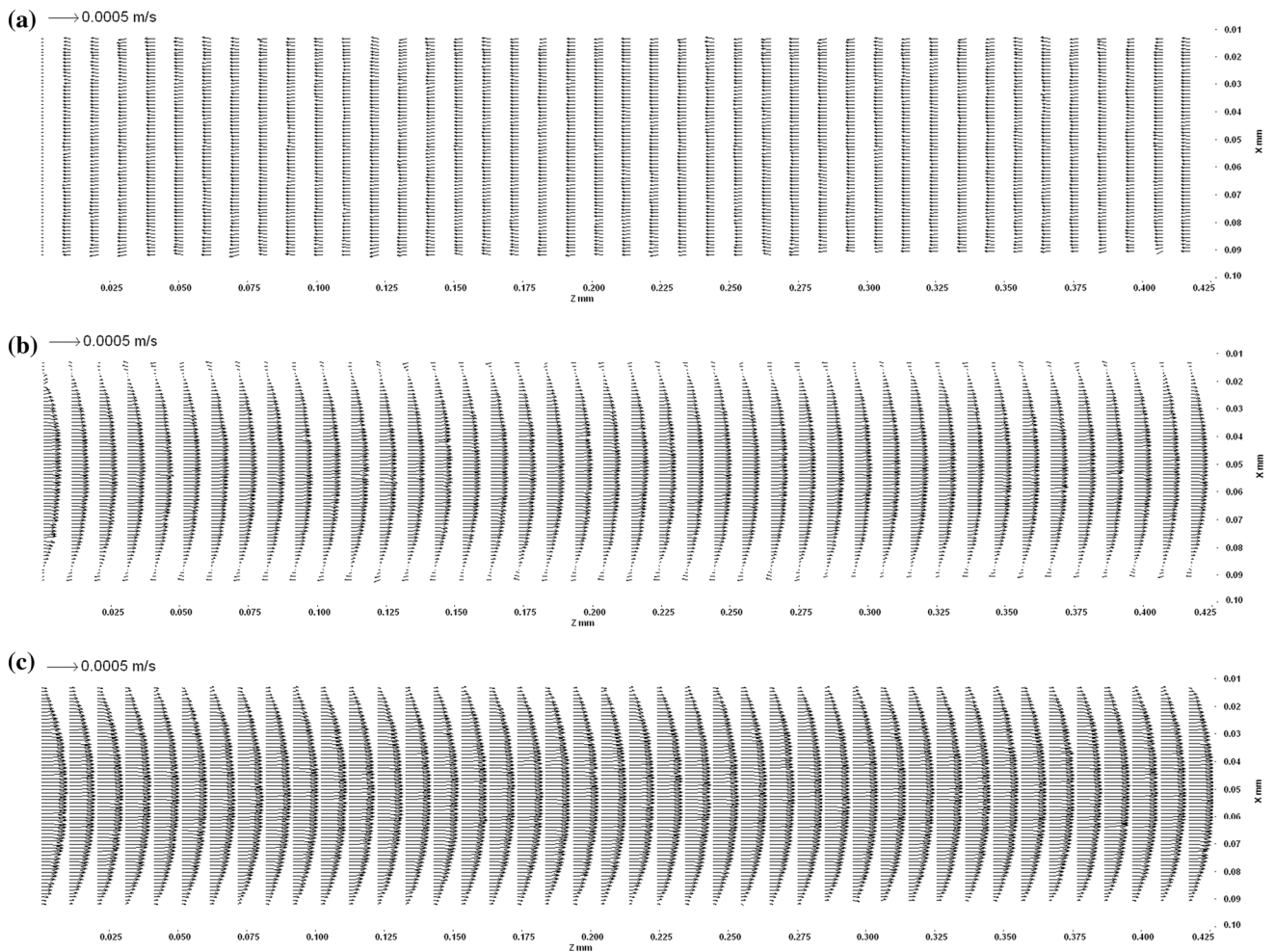**(b)** ⟶0.0005 m/s

(c) ⟶0.0005 m/s

Fig. 5 Typical velocity fields obtained in the case of **a** pure electroosmotic flow, **b** combined electroosmotic and pressure-driven flow, and **c** pure pressure-driven flow

Fig. 6 Typical surface plot of the velocity profiles $u(x, t)$ obtained by averaging the velocity profiles along the channel (i.e. in z direction). Period = 30 s (15 s on, 15 s off), applied potential = 100 V. $R_{res} = 250\,\mu m$
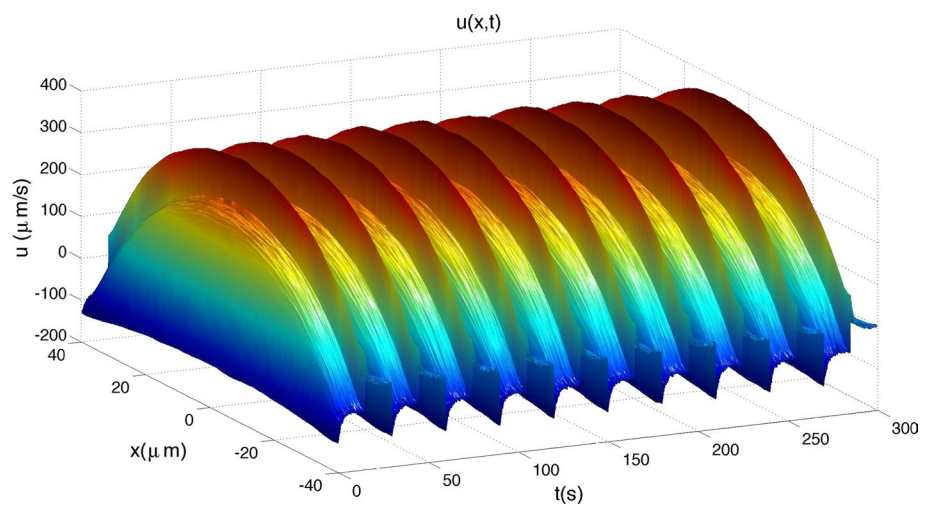
surface tension and the contact angle θ_c. We have measured the interface surface tension of the solution used in the experiments (the seeding microparticles are provided in a solution with "trace" amount of surfactant, which is then diluted in deionised water) obtaining $\Gamma = 66\,\text{mN}/\text{m}$, which is slightly lower than the typical value for water at
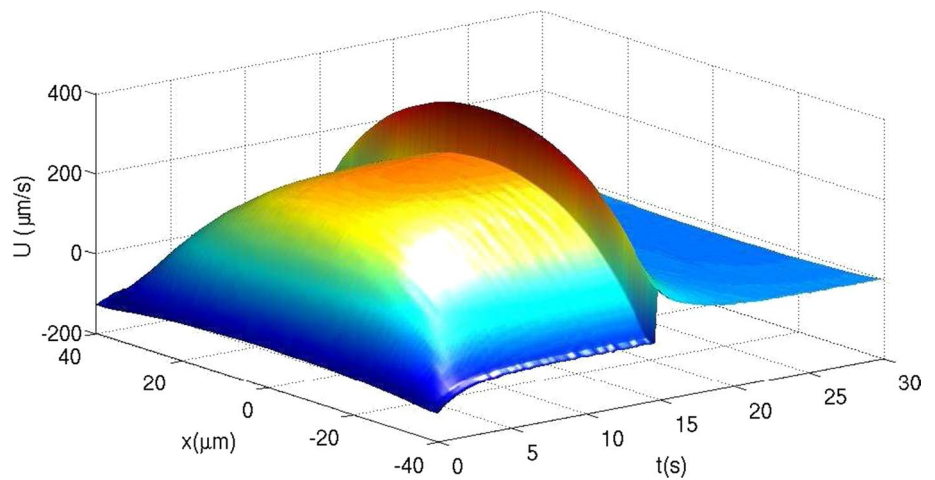
25°, $\Gamma = 72$ mN/m. At the same time, we measured the static contact angle θ_c of that solution with PDMS, obtaining $\theta_c = 89°$.

Figure 9 shows the time constants in a semi-logarithmic scale for all the reservoir diameters studied. As mentioned previously, for each reservoir diameter, the experiment consisted of a series of periods during which the potential was applied at a duty cycle of 50 %. The error bars in Figs. 9 and 10 were obtained from fitting the velocity plots for each period, during the half period with an applied potential, and during the half period without an applied potential. The average time constants and the error bars were obtained from that set of time constants. The difference between the Laplace pressures model and the experimental results ranges between 90 and 10 %. The height change model over predicts the time constants with much bigger error, between 7000 and 34,000 %. Therefore, even though neither model predicts the right values for the time constants, the one introduced in this work is clearly closer to the experimental results. The Bond number, $Bo = \Delta\rho g R_{res}^2/\Gamma$, is a dimensionless number that allows to compare the surface tension forces to the body forces ($\Delta\rho = \rho_{liquid} - \rho_{gas}$). A high value of the Bond number indicates that the system is relatively unaffected by surface tension effects; a low value (typically less than one) indicates that surface tension dominates. Intermediate numbers indicate a nontrivial balance between the two effects. In our set of experiments, with 0.150 mm $< R_{res} < 1$ mm, we get $0.0033 < Bo < 0.148$ confirming that the surface tension forces dominate. A reservoir radius of $R_{res} = 2.6$ mm would be necessary for the Bond number to reach unity, where both effects would compete. For bigger reservoir diameters, the syphoning model will be more and more accurate.

Finally, Fig. 10 presents the experimental time constants, together with the ones obtained with the Laplace pressures model. For our experimental set-up, we obtain $\tau = 189.9 R_{res}^4$ from the model (with R_{res} in mm, and τ in

s). Fitting our experimental data with a power law gives: $\tau = 268.3 R_{res}^4$, showing that the time constant varies in fact with R_{res}^4 and not with R_{res}^2 as predicted by the ΔH model. It would seem, however, that the phenomenon lies in between both models.

The model presented herein relies on the hypothesis that the interface contact line (the triple line) does not move. For a moving interface, the contact angle facing fresh surface (larger contact angle) is known as the advancing contact angle, while the contact angle moving over surface which had already been wet by the liquid (smaller contact angle) is denoted as the receding contact angle (Spori 2010). In order for the "fixed contact line" hypothesis to be valid, the contact angles between the interface and the solid surface must remain between the advancing and receding angles. A complete review on contact angle measurement and theory can be found in Spori (2010), where it is shown that the advancing contact angle is generally similar to the static contact angle, but the receding contact angle is several tens of degrees lower, particularly in the case of untreated PDMS with water. It is also shown that advancing (receding) contact angles increase (decrease) with increasing contact line speed (which can be correlated with flowrate). As mentioned previously, we measured the static contact angle and obtained $\theta_c = 89 \pm 1.5°$. We also performed measurements of the advancing and receding contact angle between our solution and native PDMS and obtained $\theta_{ca} = 91 \pm 1.5°$ and $\theta_{cr} = 48.3 \pm 1.2°$, respectively.

For a given electroosmotic velocity and microchannel dimensions, the equilibrium pressure difference is such that the net flowrate is zero. That is, it is independent of the reservoirs dimensions. In our model, such a pressure difference is dictated only by the interface curvature radius. The contact angle for that curvature radius is related to the reservoir radius R_{res} through Eq. 12, so that for a fixed curvature radius, smaller reservoir diameters will have smaller equilibrium contact angles. Concerning our experimental set-up, starting at a
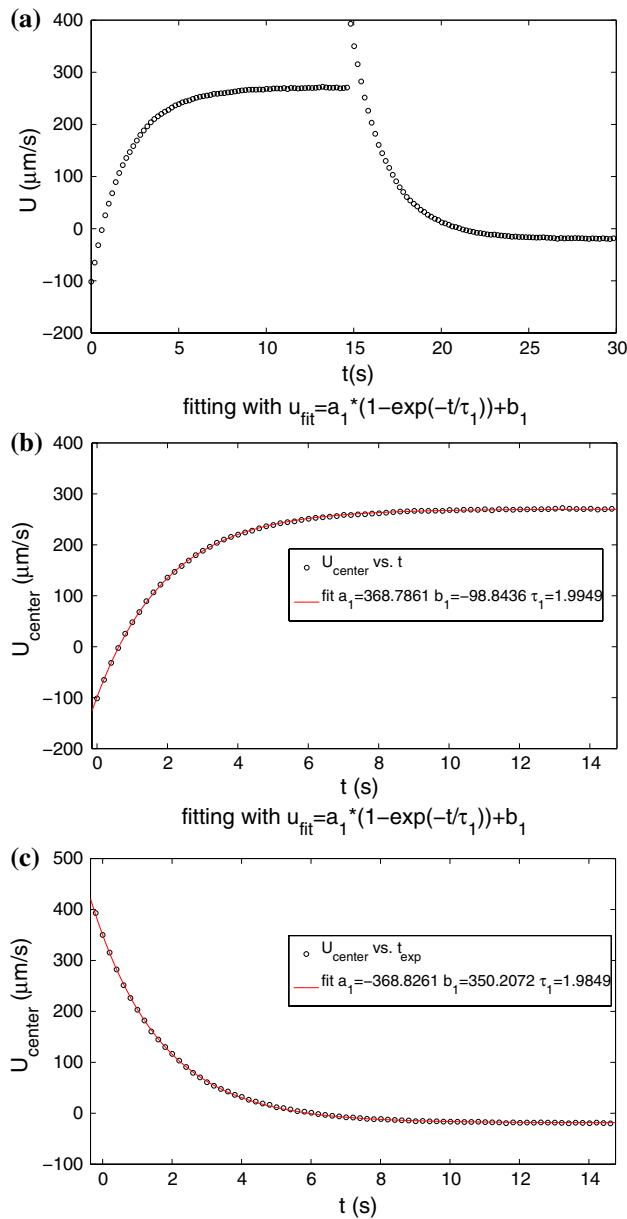
(a) fitting with $u_{fit}=a_1*(1-\exp(-t/\tau_1))+b_1$

(b) fitting with $u_{fit}=a_1*(1-\exp(-t/\tau_1))+b_1$

U_{center} vs. t

fit $a_1=368.7861$ $b_1=-98.8436$ $\tau_1=1.9949$

(c)

U_{center} vs. t_{exp}

fit $a_1=-368.8261$ $b_1=350.2072$ $\tau_1=1.9849$

Fig. 8 Experimental velocity at the channel centre. **a** Entire period. **b** First half period and exponential interpolation. **c** Second half period and exponential interpolation
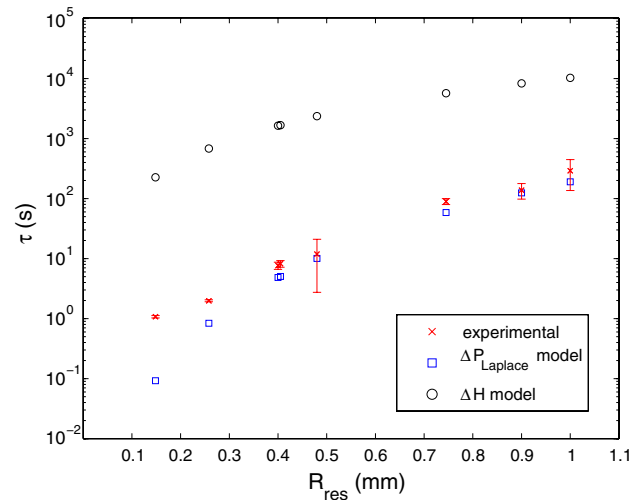

Fig. 9 Experimental and theoretical time constants (in seconds) for the different reservoir radii (R_{res}) used in this work. The $\Delta P_{Laplace}$ model shows better agreement with experimental results
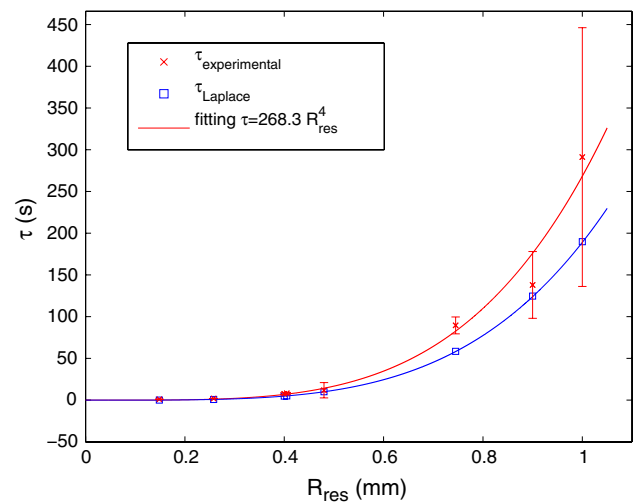

Fig. 10 Experimental and theoretical time constants (in seconds) for the different reservoir radii (R_{res}) used in this work, fitted with a power law

Table 1 Experimental and theoretical time constants (in seconds) for three different reservoir radii (R_{res}) among the ones used in this work

Experimental/model	150 μm	400 μm	745 μm
Experimental	1.1	8.2	76.8
$\Delta P_{Laplace}$ Model	0.1	4.6	53
Yan et al. (2007)	225.9	1672.4	5687

contact angle of 89°, the equilibrium contact angles modelled (for a fixed contact line) range from 90.14° for the smallest diameter (300 μm) to 96.6° for the biggest diameter (2000 μm). Therefore, for the smaller diameters the contact angle does not overcome the measured advancing contact angle. The bigger ones, however, do overcome that limiting value. We have introduced this limitation into the numerical model through a condition that forces the interface (e.g. the contact line) to start

rising/descending when the advancing/receding contact angles are reached. This does indeed increase the time constant. In our experiments, however, several periods were recorded consecutively. If the model is run for several periods, the effect of limiting the advancing/receding contact angles is visible only during one or two periods, after which the contact angle at rest (without an applied electric field, and no flow) will no longer be 89°, but a smaller angle. This can be explained as follows: hysteresis between advancing and receding contact angles allows for the contact line of the reservoir receiving the flow to start rising at a certain point (once the advancing contact angle is reached) until equilibrium occurs. At that point, if the electric field is turned off, the flow starts going in the opposite direction reducing the volume of fluid of that reservoir, but the contact line stays fixed unless the contact angle reaches the receding contact angle. With the dimensions of our experiments, this last condition was never attained. After the first period, the contact lines practically do not move any more. From then on, the time constant is slightly higher than the one for the simpler model (with a fixed contact line) because the contact angle at rest is lower than the initial contact angle (89°). As it is discussed in "Appendix", lower contact angles at rest exhibit longer time constants.

According to this discussion, smaller diameter reservoirs should present better agreement with the experiments than the bigger ones. The opposite is observed in terms of relative error. Therefore, we have also modelled a mixed Laplace + syphoning model, allowing an "arbitrary" percentage of the flowrate to produce a height change (without any of the previous considerations concerning the advancing and receding contact angles) and the rest to produce a change in the curvature radius. The percentage that allows to match the experimental results with the model ranges from 91 % (for $R_{res} = 150\,\mu m$) to 18 % (for $R_{res} = 745\,\mu$ m). That is, some of the flowrate goes to modify the interface, and the rest produces a height change. This height change will not be important in terms of pressure change (compared to the pressures produced by the interface curvature), but will allow for slower dynamics. Further research is needed to explain the differences between the experiments and the Laplace model. Nevertheless, this model is orders of magnitude closer to experimental results than the syphoning model for the reservoir diameters studied in this work.

5 Conclusions

Adverse pressure-driven backflows appear when an electroosmotic flow is imposed between two reservoirs. These backflows degrade the expected plug velocity profile and can eventually lead to zero net flowrate. Up to this date, the only model attempting to reproduce the dynamics of this phenomenon was based on the hydrostatic pressure gradient due to the height difference established by the flow, between the interfaces at the reservoirs. Some authors mention the importance of the radii of curvature of the interface on the adverse pressure gradients; however, no model based on Laplace pressure jump across the interface was developed. In this work, we introduced such a model. A simple numerical scheme has been presented to solve the system. Also, an analytical solution has been found to the linearised differential equation. According to this model, the time constant associated with this problem is proportional to R_{res}^4, as opposed to the height difference model, in which it is proportional to R_{res}^2. Our experimental results show that the time constant is indeed proportional to R_{res}^4. For the reservoir radii used in our set-up, the Laplace pressures model produces highly more accurate time constants, compared to the height change model. It seems, however, that a mixed model would reproduce the experimental dynamics better than each of the models individually.

Appendix

Curvature radii at the reservoir (solution to Eq. 13)

From Eq. 13,

$$R_{curv_j}^3 - \frac{\pi R_{res}^4}{4 vol_j} R_{curv_j}^2 - \left(\frac{3 vol_j}{4\pi} + \frac{\pi R_{res}^6}{12 vol_j} \right) = 0.$$

Replacing $\xi = R_{curv_j}/R_{res}$ and $a = 2\pi R_{res}^3/(3 vol_j)$ gives:

$$\xi^3 - \frac{3a}{8}\xi^2 - \left(\frac{1}{2a} + \frac{a}{8} \right) = 0.$$

The previous equation has one real solution which is:

$$\xi = \frac{1}{8}\left[\frac{\sqrt[3]{f(a)}}{a} + \frac{a^3}{\sqrt[3]{f(a)}} + a \right],$$

with

$$f(a) = 128a^2 + 32a^4 + a^6 + 8a^2\sqrt{256 + 128a^2 + 20a^4 + a^6}.$$

Numerical solution to Eq. 16

From Eq. 16,

$$q(t) = q_{EOF} - K_2 \left(\frac{1}{R_{curv_1}(t)} - \frac{1}{R_{curv_2}(t)} \right),$$

$$K_2 = 2K_1\Gamma.$$

This equation can be solved numerically following the next sequence of operations,

$$q_{\nabla p}{}^0 = 0 \;\rightarrow\; q^0 = q_{\text{EOF}},$$

$$vol_1{}^n = vol_1^{(n-1)} + q^{(n-1)}\mathrm{d}t \;\rightarrow\; a_1{}^n = \frac{2\pi R_{\text{res}}^3}{3vol_1{}^n},$$

$$vol_2{}^n = vol_2^{(n-1)} - q^{(n-1)}\mathrm{d}t \;\rightarrow\; a_2{}^n = \frac{2\pi R_{\text{res}}^3}{3vol_2{}^n},$$

$$\xi_1{}^n = \frac{1}{8}\left[\frac{\sqrt[3]{f(a_1{}^n)}}{a_1{}^n} + \frac{(a_1{}^n)^3}{\sqrt[3]{f(a_1{}^n)}} + a_1{}^n\right],$$

$$\xi_2{}^n = \frac{1}{8}\left[\frac{\sqrt[3]{f(a_2{}^n)}}{a_2{}^n} + \frac{(a_2{}^n)^3}{\sqrt[3]{f(a_2{}^n)}} + a_2{}^n\right],$$

$$q_{\nabla p}{}^n = -\frac{K_2}{R_{\text{res}}}\left(\frac{1}{\xi_1{}^n} - \frac{1}{\xi_2{}^n}\right),$$

$$q^n = q_{\text{EOF}} + q_{\nabla p}{}^n,$$

$$t^n = n\,\mathrm{d}t.$$

Analytical solution to Eq. 16

To compare our model to the one based on the height difference presented by Yan et al. (2007), Eq. 16 may be simplified. First, we rewrite it using some of the definitions from "Appendix", and considering that both reservoirs are identical in shape and material:

$$vol_1(t) = vol_1(0) + \int_0^t q(t)\,\mathrm{d}t = vol_0 + Q(t),$$

$$vol_2(t) = vol_2(0) - \int_0^t q(t)\,\mathrm{d}t = vol_0 - Q(t),$$

using $C = \frac{2\pi R_{\text{res}}^3}{3}$, we can write:
$a_1(t) = \frac{C}{vol_0+Q(t)};\quad a_2(t) = \frac{C}{vol_0-Q(t)}$, then,

$$\xi_1(t) = \xi\left(\frac{C}{vol_0+Q(t)}\right);\quad \xi_2(t) = \xi\left(\frac{C}{vol_0-Q(t)}\right),$$

$$q(t) = q_{\text{EOF}} - \frac{K_2}{R_{\text{res}}}G(Q(t)),$$

$$G(Q(t)) = \frac{1}{\xi\left(\frac{C}{vol_0+Q(t)}\right)} - \frac{1}{\xi\left(\frac{C}{vol_0-Q(t)}\right)},$$

with $Q(0) = 0$.

Then we write the Taylor series of $G(Q)$ about $Q(0) = 0$:

$$G(Q) = G(0) + \left.\frac{\mathrm{d}G}{\mathrm{d}Q}\right|_{Q=0} Q + \left.\frac{\mathrm{d}^2 G}{\mathrm{d}Q^2}\right|_{Q=0} Q^2 + \cdots + R_n.$$
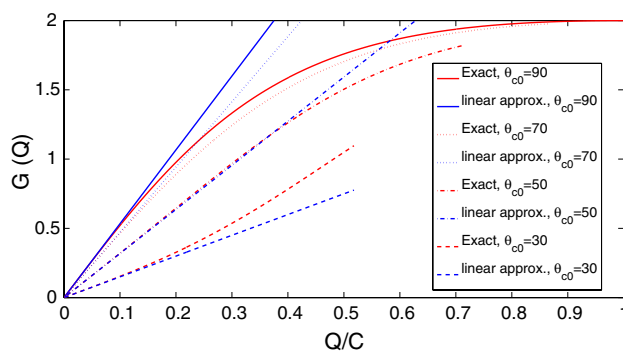
where:

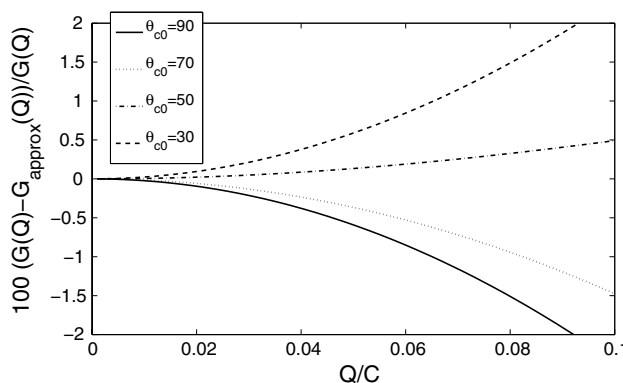**Fig. 11** Approximate solution of $G(Q)$ together with the exact solution for different equilibrium contact angles θ_{c0}

Fig. 12 Relative error between the exact and approximated solution of the function $G(Q)$

$$G(Q = 0) = 0,$$

$$\left.\frac{\mathrm{d}G}{\mathrm{d}Q}\right|_{Q=0} = \frac{16}{3C}H\big(a|_{Q=0}\big),$$

$$a|_{Q=0} = a_0 = \frac{C}{vol_0} = \frac{2\pi R_{\text{res}}^3}{3\,vol_0},$$

$$H(a) = \frac{\frac{1}{a^5}\frac{\mathrm{d}f}{\mathrm{d}a} - \frac{3f(a)}{a^6} + \frac{9f(a)^{\frac{1}{3}}}{a^2} - \frac{f(a)^{-\frac{2}{3}}}{a}\frac{\mathrm{d}f}{\mathrm{d}a} + \frac{3f(a)^{\frac{2}{3}}}{a^4}}{1 + \frac{3f(a)^{\frac{2}{3}}}{a^4} + \frac{2f(a)}{a^6} + \frac{2f(a)^{\frac{1}{3}}}{a^2} + \frac{f(a)^{\frac{4}{3}}}{a^8}},$$

$$\frac{\mathrm{d}f}{\mathrm{d}a} = 256\,a + 128\,a^3 + 6\,a^5$$

$$+ \frac{4096\,a + 3072\,a^3 + 640\,a^5 + 40\,a^7}{\sqrt{256 + 128\,a^2 + 20\,a^4 + a^6}}.$$
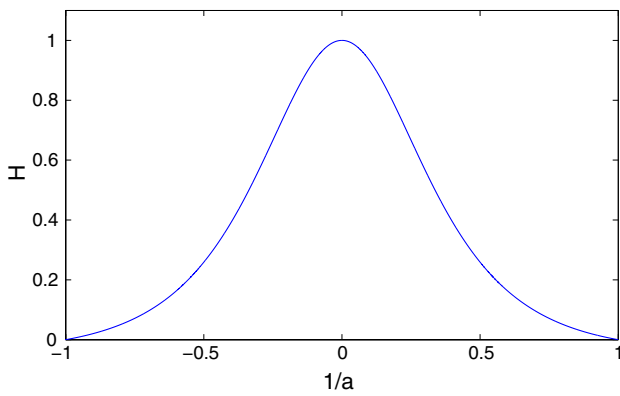
Therefore, a first-order approximation gives

Fig. 13 Function H versus the relative volume $1/a_0 = vol_0/C$

Fig. 14 Exact (numerical) result of $q(t)$ to the linearised solution, for different equilibrium contact angles θ_{c0}

$$G(Q) = \frac{16}{3C}H(a_0)Q(t),$$

$$q(t) = q_{\text{EOF}} - \frac{1}{\tau}\int_0^t q(t)\,dt,$$

with $\tau = \dfrac{2\pi R_{\text{res}}{}^4 \mu L F\left(\frac{h}{b}\right)}{H(a_0)\Gamma D_h{}^2 bh}.$

The solution to the previous equation is:

$$q(t) = q_{\text{EOF}} \exp\left(-\frac{t}{\tau}\right).$$

Analysis of the exact and linearised solutions

Figure 11 shows the approximate solution of $G(Q)$ together with the exact solution for different initial volumes vol_0 (i.e. for different equilibrium contact angles θ_{c0}). It should be noted that the maximum value of Q/C is equal to $1 - vol_0/C$, because the radius of curvature of the interface cannot be lower than the reservoir radius. In this figure, it is clear that the linear solution is valid only for a small portion of the curve around $Q/C = 0$, or, in other words, for small deformations of the interface.

Figure 12 shows that the relative error between the exact and approximated solution of the function $G(Q)$ is below 2 % for transported volumes lower than 9 % of the maximum volume (i.e. C: half the volume of a sphere with radius R_{res}), for equilibrium contact angles $\theta_{c0} > 30°$.

The function $H(a_0)$ can be represented versus the relative volume $1/a_0 = vol_0/C$. The result is presented in Fig. 13. The function varies between ~0 for initial volumes equal to the maximum volume C ($\theta_c = 0°$, $a = 1$) and 1 for null initial volumes ($\theta_c = 90°$, $a \to \infty$). When looking at the characteristic time constant τ, one can see that it is proportional to $1/H(a_0)$. That means that, according to the linearised solution, a liquid wetting the reservoir's walls will have a longer time constant than a liquid not wetting them.
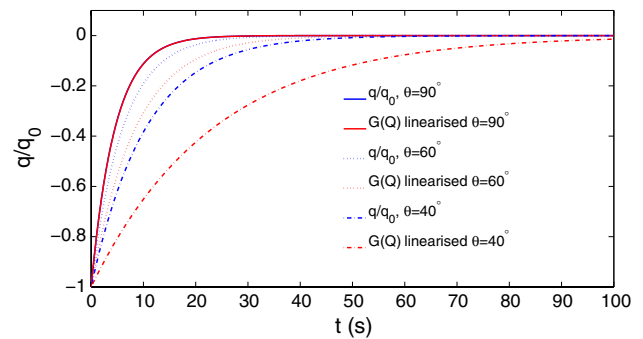
Finally, in Fig. 14 we compare the exact (numerical) result of $q(t)$ to the linearised solution, for different initial volumes vol_0. It can be observed that the linearised solution predicts longer time constants than the exact solution and that the difference between both time constants increases as the initial volume vol_0 increases. For small initial volumes (i.e. for contact angles close to 90°), however, the time constant obtained with the linearised solution remains a very good estimate of the exact time constant of this model.

References

Arthur APG, Adamson W (1997) Physical chemistry of surfaces, 6th edn. Wiley. http://gen.lib.rus.ec/book/index.php?md5=F5D731FC6ED5F095C530DA0C28C040AD

Bourdon CJ, Olsen MG, Gorby AD (2004) Validation of an analytical solution for depth of correlation in microscopic particle image velocimetry. Meas Sci Technol 15(2):318

Burgreen D, Nakache FR (1964) Electrokinetic flow in ultrafine capillary slits1. J Phys Chem 68(5):1084. doi:10.1021/j100787a019

Crabtree HJ, Cheong ECS, Tilroe DA, Backhouse CJ (2001) Microchip injection and separation anomalies due to pressure effects. Anal Chem 73(17):4079. doi:10.1021/ac010217r

Duffy CF, McEathron AA, Arriaga EA (2002) Determination of individual microsphere properties by capillary electrophoresis with laser-induced fluorescence detection. Electrophoresis 23(13):2040

Dutta P, Beskok A (2001) Analytical solution of combined electroosmotic/pressure driven flows in two-dimensional straight channels: finite Debye layer effects. Anal Chem 73(9):1979. doi:10.1021/ac001182i

Ghosal S (2004) Fluid mechanics of electroosmotic flow and its effect on band broadening in capillary electrophoresis. Electrophoresis 25(2):214. doi:10.1002/elps.200305745

Hunter RJ (2001) Foundations of colloid science, 2nd edn. Oxford University Press, Oxford

Kirby BJ (2010) Micro- and nanoscale fluid mechanics, transport in microfluidic devices, 1st edn. Cambridge University Press, Cambridge

Kirby BJ, Hasselbrink EF (2004) Zeta potential of microfluidic substrates: 2. Data for polymers. Electrophoresis 25(2):203

Kirby BJ, Hasselbrink EF (2004) Zeta potential of microfluidic substrates: 1. Theory, experimental techniques, and effects

on separations. Electrophoresis 25(2):187. doi:10.1002/elps.200305754

Li D (2004) Electrokinetics in microfluidics. In: Li D (ed) Interface science and technology, vol 2. Elsevier, pp 92–203. doi:10.1016/S1573-4285(04)80026-7. http://www.sciencedirect.com/science/article/pii/S1573428504800267

Lyklema JJ, de Keizer A, Bijsterbosch B, Fleer G, M.C.S. (ed) (1995) Solid-liquid interfaces, fundamentals of interface and colloid science, vol 2. Elsevier, Academic Press, Cambridge

MacInnes JM, Du X, Allen RWK (2003) Prediction of electrokinetic and pressure flow in a microchannel T-junction. Phys Fluids 15(7):1992. doi:10.1063/1.1580479

Marcos C, Yang TN, Wong KT, Ooi (2004) Dynamic aspects of electroosmotic flow in rectangular microchannels. Int J Eng Sci 42(1314):1459. doi:10.1016/j.ijengsci.2003.07.012. http://www.sciencedirect.com/science/article/pii/S0020722504001028

Santiago JG, Wereley ST, Meinhart CD, Beebe DJ, Adrian RJ (1998) A particle image velocimetry system for microfluidics. Exp Fluids 25(4):316. doi:10.1007/s003480050235

Santiago JG (2001) Electroosmotic flows in microchannels with finite inertial and pressure forces. Anal Chem 73(10):2353. doi:10.1021/ac0101398

Sinton D, Ren L, Li D (2003a) Visualization and numerical modelling of microfluidic on-chip injection processes. J Colloid Interface Sci 260(2):431. doi:10.1016/S0021-9797(02)00181-9. http://www.sciencedirect.com/science/article/pii/S0021979702001819

Sinton D, Ren L, Li D (2003b) A dynamic loading method for controlling on-chip microfluidic sample injection. J Colloid Interface Sci 266(2):448. doi:10.1016/S0021-9797(03)00630-1. http://www.sciencedirect.com/science/article/pii/S0021979703006301

Söderman O, Jönsson B (1996) Electro-osmosis: velocity profiles in different geometries with both temporal and spatial resolution. J Chem Phys 105(23):10300. doi:10.1063/1.472958

Spori DM (2010) Structural influences on self-cleaning surfaces. Ph.D. thesis, ETH Zurich

Spurk J, Aksel N (2007) Fluid mechanics, 2nd edn. Springer, Berlin

Squires TM, Quake SR (2005) Microfluidics: fluid physics at the nanoliter scale. Rev Mod Phys 77:977. doi:10.1103/RevModPhys.77.977

Sze A, Erickson D, Ren L, Li D (2003) Zeta-potential measurement using the Smoluchowski equation and the slope of the current–time relationship in electroosmotic flow. J Colloid Interface Sci 261(2):402

Venditti R, Xuan X, Li D (2006) Experimental characterization of the temperature dependence of zeta potential and its effect on electroosmotic flow velocity in microchannels. Microfluid Nanofluidics 2(6):493

Wereley ST, Meinhart CD (2010) Recent advances in micro-particle image velocimetry. Annu Rev Fluid Mech 42(1):557. doi:10.1146/annurev-fluid-121108-145427

Xiong B, Pallandre A, le Potier I, Audebert P, Fattal E, Tsapis N, Barratt G, Taverna M (2012) Electrophoretic mobility measurement by laser Doppler velocimetry and capillary electrophoresis of micrometric fluorescent polystyrene beads. Anal Methods 4(1):183

Yan D, Yang C, Nguyen NT, Huang X (2006) A method for simultaneously determining the zeta potentials of the channel surface and the tracer particles using microparticle image velocimetry technique. Electrophoresis 27(3):620

Yan D, Yang C, Huang X (2007) Effect of finite reservoir size on electroosmotic flow in microchannels. Microfluid Nanofluidics 3(3):333. doi:10.1007/s10404-006-0135-2